Engineering Photoresponse in Epitaxial $BiFe_{0.5}Cr_{0.5}O_3$ Thin Films through Structural Distortion

*Mohammad Moein Seyfouri,[1] Dawei Zhang,[1] César Menéndez,[2] Daniel Sando,[1,3,4], Qi Zhang,[1] Claudio Cazorla,[5] Jan Seidel,[1,4] and Danyang Wang[1]**

[1] School of Materials Science and Engineering, UNSW Sydney, NSW 2052, Australia

[2] School of Chemistry, The University of Sydney, NSW 2006, Australia

[3] Solid State and Elemental Analysis Unit, Mark Wainwright Analytical Centre, UNSW Sydney, NSW 2052, Australia

[4] ARC Centre of Excellence in Future Low-Energy Electronics Technologies (FLEET), UNSW Sydney, NSW 2052, Australia

[5] Department de Física, Universitat Politècnica de Catalunya, Barcelona 08034, Spain

* Email: dy.wang@unsw.edu.au

1. Surface Morphology

The growth mode of the epitaxial BFCO film was inferred by observing the surface morphology. The SRO buffer layer demonstrates an atomically smooth surface (rms=0.3 nm) and preserves the overall structure of the as-received STO stepped substrate, as shown in Figure S1.

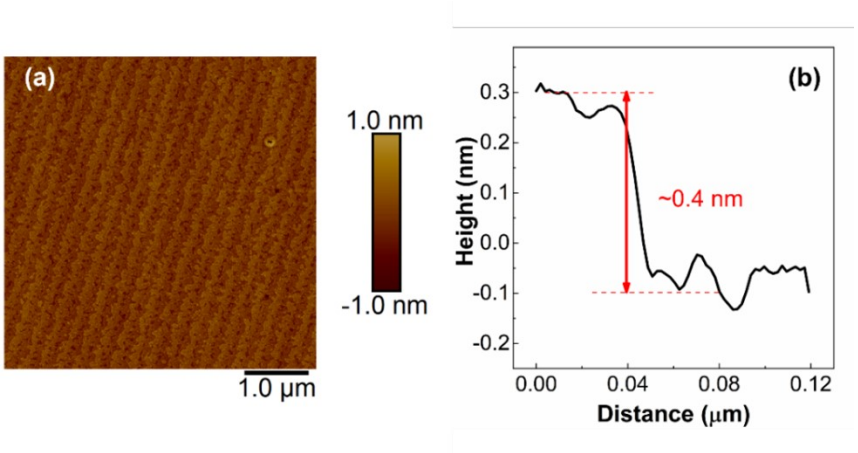

Figure S1 (a) AFM image of 12 nm-thick SRO buffer layer (b) Step line profile extracted from AFM image using NanoScope software

Figure S2 confirms that all BFCO layers exhibited an island-like morphology consistent with the 3D growth mode. Our result indicates that BFCO might follow the island mode from the very early growth stage due to the high nucleation density, or the 2D layer-by-layer (LBL) growth occurs up to a certain thickness before transitioning to the 3D island mode. The latter behaviour is more plausible since LBL growth of coherent ultrathin BFCO films only up to a few nm was reported earlier, where stringent processing conditions had to be applied, e.g. very low growth rate and judicious choice of vicinal substrate.[1] Therefore, one can assume that the BFCO/SRO/STO heteroepitaxy can be a representative case of Stranski-Krastanov growth, for which the corresponding surface roughening is due to the elastic forces imparted by the underlying substrate.[2]

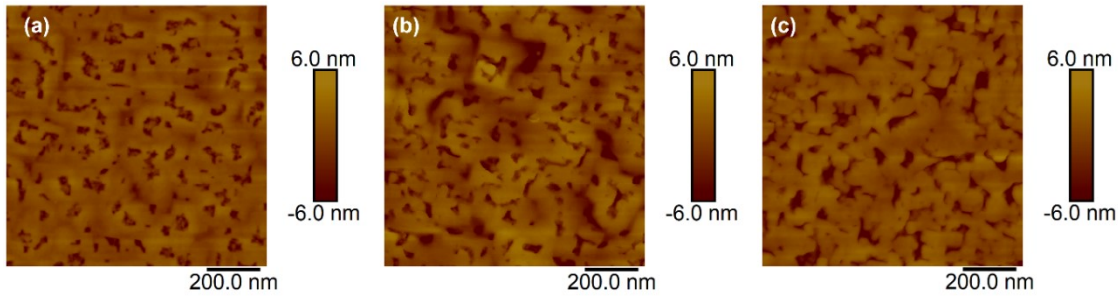

Figure S2 AFM images of (a) 30 nm (b) 70 nm (c) 130 nm -thick BFCO films grown on SRO-buffered STO

2. Rocking curve scan

Figure S3 shows the narrow FWHM of omega scan around 002 reflection, which confirms the high crystalline quality of all three samples.

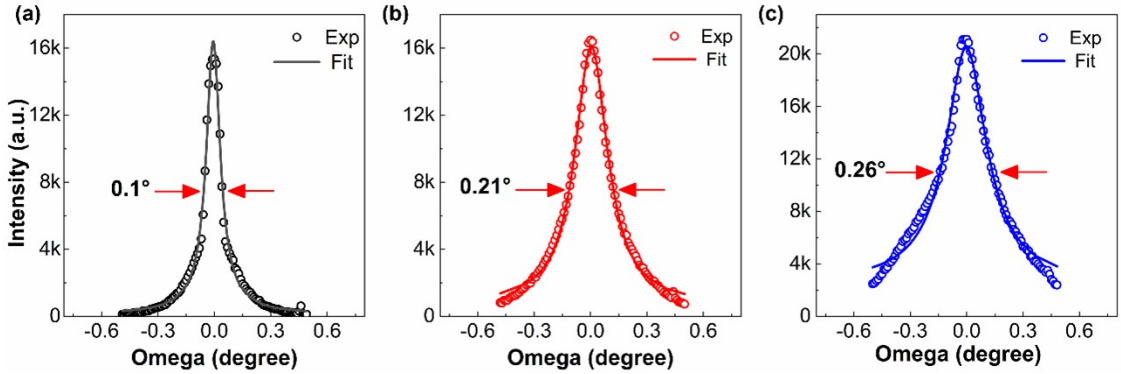

Figure S3 Rocking curves around $(002)_{pc}$ BFCO peak of (a) 30 (b) 70 and (c) 130 nm films.

3. Film thickness measurement

XRR patterns for all samples exhibited a multitude of oscillations depending on the thickness of the layer. Fitting the reflectometry data using a genetic algorithm yielded the thickness of layers in the heterostructure, as presented in Table S1.

Table S1 Calculated thickness from fitted XRR measurement

Sample	Thickness of layer (nm)	
	SRO	**BFCO**
1	11.50	31.30
2	11.80	71.20
3	11.40	130.00

The confidence of the results was confirmed by monitoring the error analysis. A representative image of such analysis is shown in Figure S4 for 30 nm thin film, pointing out that the fitting formula is optimised by the global solution, which minimises the absolute square root difference function.

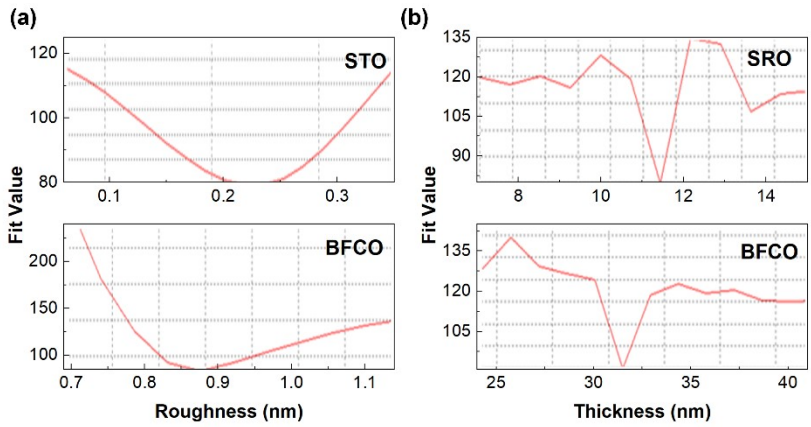

Figure S4 Regression error analysis for (a) roughness (b) thickness calculation (X'Pert Reflectivity software Ver. 1.1)

4. Critical thickness calculation

The modified Matthews-Blakeslee (MB) model can predict the critical thickness for ferroelectric thin films where strain relaxation occurs by the misfit dislocation.[3]

$$t_c/b = \left(ln(\alpha\, t_c/b)\right)/8\pi(1+\upsilon)\epsilon \qquad (\boldsymbol{Equation\ S1})$$

where b is the Burgers vector, ν is Poisson's ratio, ϵ and α denote misfit strain and cut-off parameter representing the continuum energy of the dislocation core, respectively. The Poisson's ratio was presumed to be 0.3, a typical value for BFO-based thin film on STO (001) substrate,[4] and α was set to 4.[3] Figure S5 shows how Equation (S1) is solved numerically.

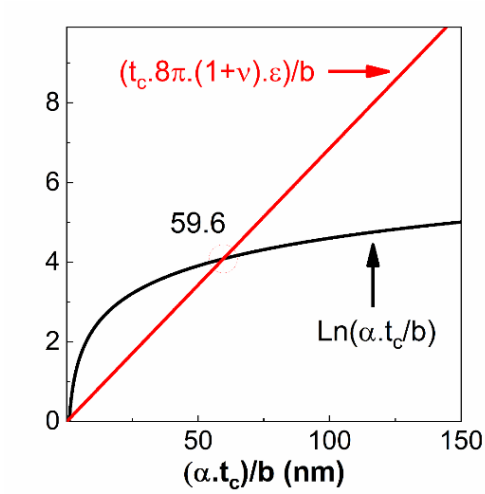

Figure S5 Numerical solution for Matthews-Blakeslee (MB) equation

5. Inhomogeneous strain calculation

Equation (S2) expresses the Williamson-Hall relation as follows:[5]

$$(\beta cos\theta)^2 = (K\lambda/D)^2 + (4\varepsilon_i sin\theta)^2 \quad (\boldsymbol{Equation\ S2})$$

where θ and β are the angle and breadth of diffraction peak, respectively, and D denotes the coherence length along the scattering vector. As shown in Figure S6, we obtained the inhomogeneous strain (ε_i) from the slope of linear fit for (00*l*) BFCO reflections—up to *l*=4— by plotting $\beta^2\cos^2(\theta)$ versus $(4\sin(\theta))^2$. The XRD peak broadening is mainly due to the finite size, inhomogeneous strain, and diffractometer resolution. For the Gaussian peak profiles, it is suggested to utilise the quadratic peak broadening equation, as expressed by $\beta^2 = {\beta_{size}}^2 + {\beta_{strain}}^2 + {\beta_{instrument}}^2$.[5] In our study, we approximated the instrumental contribution by subtracting the line width of the corresponding substrate peak. As expected, the coherence lengths (D) calculated from the intercept also showed a monotonic trend with increasing film thickness.

Note should be taken that the described quantitative analysis heavily depends on the approach taken to separate the contribution of size and strain in the linewidth broadening. Therefore, it is better to use such analysis for comparison per se. It is also highly recommended to employ other techniques such as grazing incident small angle x-ray scattering when the precise measurement of crystallite grain size is the focus of the study.

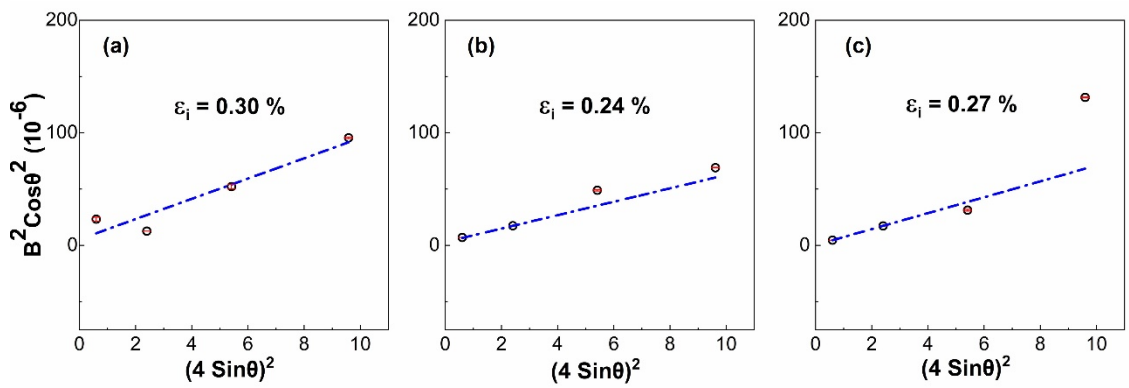

Figure S6 Williamson-Hall analysis of (a) 30 (b) 70 and (c) 130 nm films.

6. Reciprocal Space Mapping

Using XRD RSM, it is possible to determine the low symmetry phases by performing diffraction measurements in the scattering zones with a fixed (001) crystallographic axis. In other words, the highly oriented epitaxial (001) thin film simplifies the interpretation of the result as the splitting of the peak is associated with the axis perpendicular to the fixed one.[6] For instance, splitting of the Bragg peak in the H0L and HHL scattering planes that are geometrically accessible in most diffractometers is commonly utilised to resolve the monoclinic distortion.[7,8] Furthermore, unit cell parameters can be inferred from RSM graph as summarised in Figure 3a. For instance, the lattice parameters of the distorted phase were extracted from the RSM scan of 130 nm-thick film as follows: a_m = 5.59 Å, b_m = 5.50 Å and c_m = 7.94 Å with a distortion angle value of ~ 0.15°. To obtain more useful information, the average in-plane lattice parameter was also estimated using $0.5 \times \sqrt{a_m^2 + b_m^2}$ Formula.[6]

We crosschecked the possibility of single domain monoclinic tilting in 30 nm-thick film through mapping the family of (103) asymmetric Bragg peaks. Nonetheless, as shown in Figure S7, all RSM peaks came along the same OP reciprocal lattice spacing, confirming the tetragonal structure of the unit cell within the resolution of the diffractometer used herein.

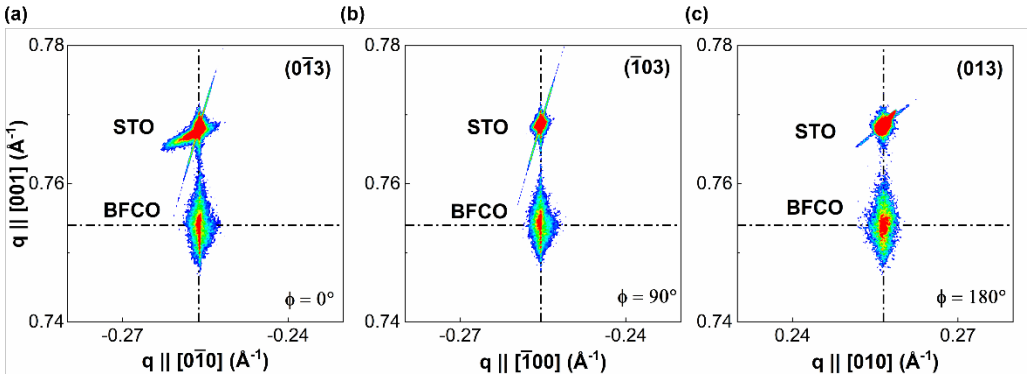

Figure S7 Asymmetric {103} RSM family plot of the 30 nm-thick BFCO film recorded along (a) [0$\bar{1}$0] (b) [$\bar{1}$00] (c) [010] via in-plane rotation of sample by 90 degrees during XRD scan.

Figure S8 demonstrates the schematic describing the tilting mechanism observed in BFCO films as the film thickness increased to 130 nm.

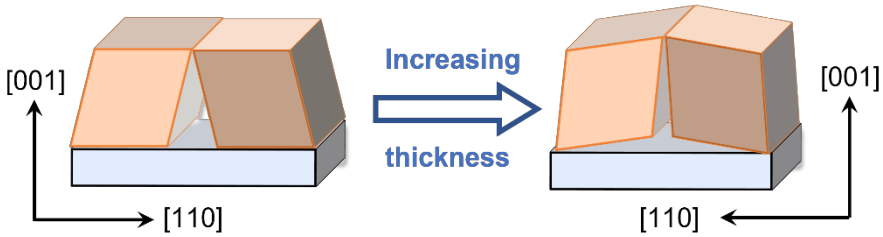

Figure S8 Schematic showing tilting of the domain as the film thickness increases

7. First-principles calculation

The calculation of the polarisation confirmed that both phases are polar with values of ~ 90 μC cm^{-2} along the [111] pseudocubic direction and along the [001] direction for the rhombohedral and the tetragonal

phase, respectively. On a side note, a third stable and competitive orthorhombic phase was also found at high compressive strain. This phase, with symmetry derived from the *Pnma* space group, was identified as centrosymmetric and hence, non-polar active. Figure S9 shows the pDOS on the individual *d*-orbitals, which confirms the presence of Fe^{3+} and Cr^{3+} species in both structures.

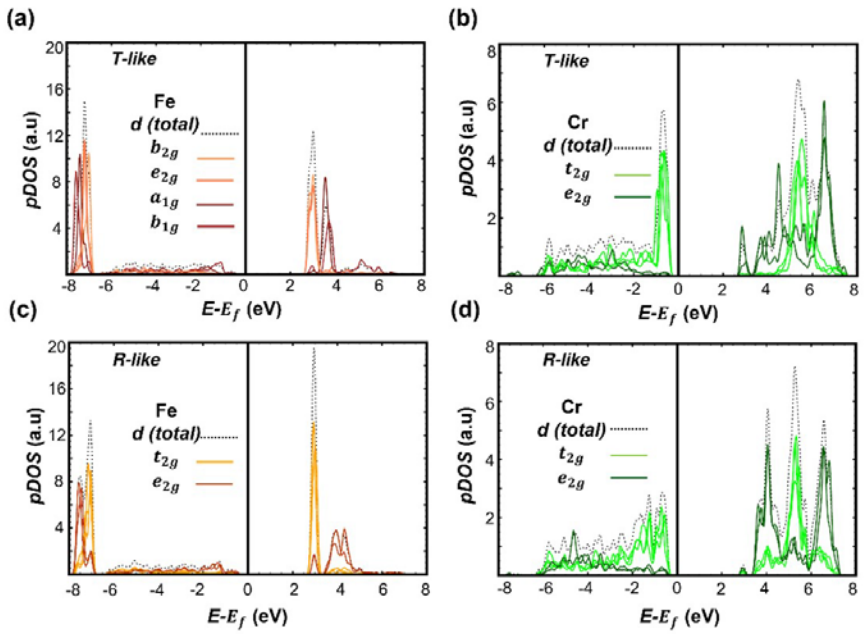

Figure S9 Projected density of states on individual d-orbitals for (a, b) T-like (c, d) R-like structure

8. XPS results

The C-1s signal of adventitious carbon (284.8 eV) is used for charge correction. As shown in Figure S10, the binding energy of the Bi-4f core level appears at 158.7 and 164.1 eV for the $4f_{7/2}$ and $4f_{5/2}$, respectively. The Bi-4f spin-orbit doublets are apart by 5.4 eV, implying an oxidation state of 3+ for bismuth.[9] The Fe-2p spectra clearly show a distinctive satellite feature at the binding energy of 719.4 eV, which is the fingerprint of Fe^{3+} ions.[10] In addition, separation of 14 eV between $2p_{3/2}$ and $2p_{1/2}$ further corroborates the prevalence of Fe^{3+} cations.[11] Nonetheless, the presence of minority Fe^{2+} states cannot be ruled out due to relatively low oxygen pressure during growth, but further investigation is not the scope of this study. The region scan around the Cr-2p spectrum exhibits $2p_{1/2}$ and $2p_{3/2}$ components at binding energies of 576.3 eV

and 586.3, respectively, consistent with a single-peak fitted trivalent Cr spectrum.[12] Of note, it is expected to observe multiplet splitting during the photoionisation process in the XPS spectra of transition metal ions if they have unpaired electrons at their core level. To confirm that the valence state of Cr species is not misinterpreted from single line-shape fitting, an in-depth characterisation of multiplet splitting can be done to elucidate the chemical state at the sample surface. The Cr-2p3/2 core level completely fits the trivalent state of chromium using a multiplet structure similar to the pattern reported in the literature.[12,13]

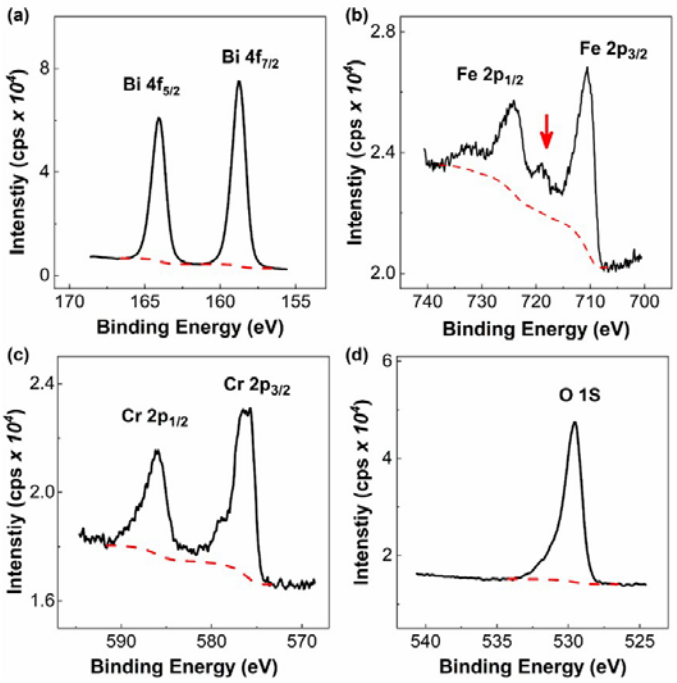

Figure S10 Representative XPS spectra for (a) Bi 4f (b) Fe 2p (c) Cr 2p (d) O 1s core levels.

Furthermore, the sharp peak at 529.6 eV in the O-1s spectrum is associated with transition metal-oxygen species in agreement with the photoelectron line position of metal oxides.[14] Table S2 summarised the centre of gravity for core-level photoemission peaks as described above.

Table S1 Binding energies of XPS peak extracted from the core level spectrum

Elements	**O (-2)**	**Bi (3+)**		**Cr (3+)**		**Fe (3+)**		
Peak	**1S**	**$4f_{7/2}$**	**$4f_{5/2}$**	**$2p_{3/2}$**	**$2p_{1/3}$**	**$2p_{3/2}$**	**$2p_{1/3}$**	**Sat. $2p_{3/2}$**
BE (eV)	529.6	158.7	164.1	576.3	586.3	710.8	724.8	719.4

9. Optical characterisation

First, the optical data for the STO substrate and SRO bottom electrode was acquired. The bandgap of STO substrate was extracted to be 3.2 eV (see Figure S11), which is in agreement with that in the literature.[15] Therefore, all the optical data for the BFCO layer were constrained to 3.2 eV, due to the substantial interference from the underlying substrate.

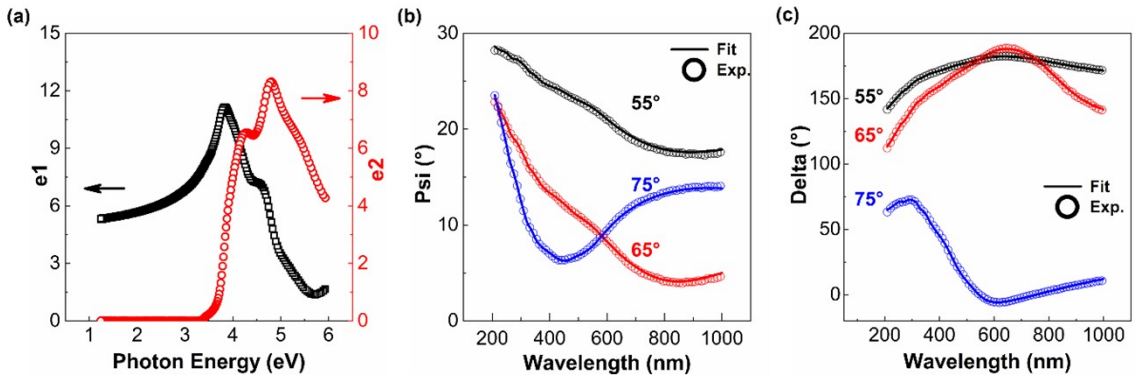

Figure S11 (a) Dielectric function of STO substrate. (b, c) Raw ellipsometry parameter of the representative BFCO film measured at three different angles.

The parameters representing these oscillators are shown in Table S3, yielding an excellent fit to the experimental data.

Table S2 Detail of the oscillators for the ellipsometry fitting procedure

	ε_1. offset	Gauss.1			Gauss.2			Gauss.3		
		Br	**En**	**Amp**	**Br**	**En**	**Amp**	**Br**	**En**	**Amp**
T-like	2.38 (±0.01)	0.50 (±0.02)	2.29 (±0.007)	0.29 (±0.01)	1.61 (±0.01)	3.98 (±0.005)	2.97 (±0.04)	3.66 (±0.01)	5.52 (±0.01)	7.01 (±0.02)
R-like	2.35 (±0.02)	0.43 (±0.02)	2.33 (±0.007)	0.25 (±0.01)	1.93 (±0.03)	3.97 (±0.01)	2.51 (±0.14)	3.39 (±0.05)	6.02 (±0.02)	8.61 (±0.03)

To ensure modulation of photon energy is the main contributor to the observed result, Figure S12 presents the on/off photoresponse at the different laser wavelengths for the R-like BFCO sample. One can assume the T-like sample behaves the same as the R-like sample since there is an apparent current increase between -2 V at the dark and 405 nm laser illumination, as shown in Figure 5c, where the current eventually falls to zero once the light source is off.

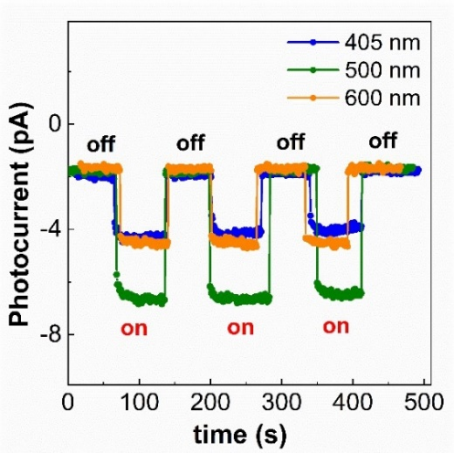

Figure S12 Time-dependent photoresponse of the R-like sample at three different wavelengths.

Figure S13 shows the laser intensity as a function of wavelength for the light source (FemtoPower 1060), which was used to illuminate the sample in the SPM measurements.

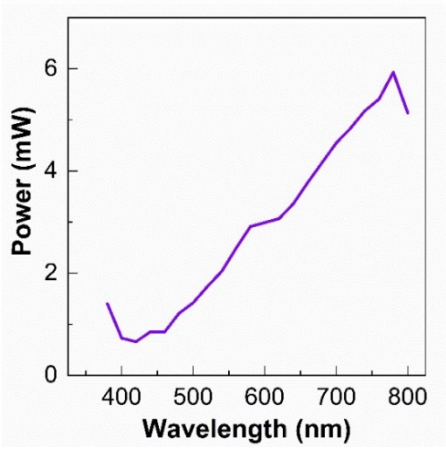

Figure S13 Laser intensity as a function of wavelength

10. Photoferroelectric Response

Figure S14 presents the KPFM and c-AFM images for both samples. In this configuration, the bottom half of the image was recorded in the dark, while the top half represents the measurement during exposure to the laser source in order to alleviate the impact of severe polarisation back switching in the T-like structure during the measurement.

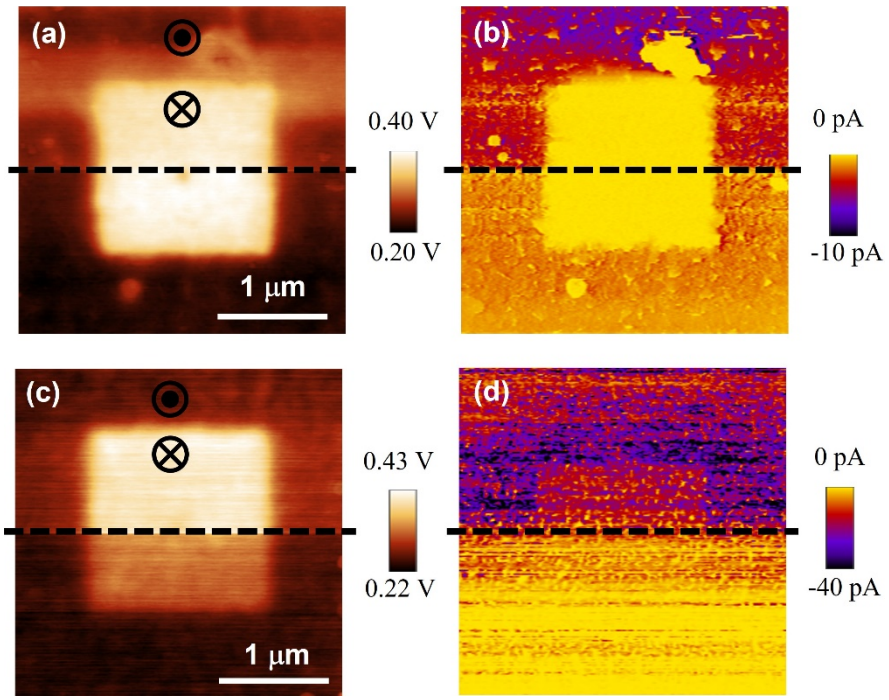

Figure S14 KPFM and c-AFM mapping for (a-b) R-like (c-d) T-like BFCO film. (Top half is under UV illumination (405 nm = 3 eV) and the bottom half is in the dark)

References

(1) Nechache, R.; Harnagea, C.; Rosei, F. Multiferroic Nanoscale Bi_2FeCrO_6 Material for Spintronic-Related Applications. *Nanoscale* **2012**, *4* (18), 5588. https://doi.org/10.1039/c2nr31429k.

(2) Solmaz, A.; Huijben, M.; Koster, G.; Egoavil, R.; Gauquelin, N.; Van Tendeloo, G.; Verbeeck, J.; Noheda, B.; Rijnders, G. Domain Selectivity in $BiFeO_3$ Thin Films by Modified Substrate

Termination. *Adv. Funct. Mater.* **2016**, *26* (17), 2882–2889. https://doi.org/10.1002/adfm.201505065.

(3) Venkatesan, S.; Vlooswijk, A.; Kooi, B. J.; Morelli, A.; Palasantzas, G.; De Hosson, J. T. M.; Noheda, B. Monodomain Strained Ferroelectric $PbTiO_3$ Thin Films: Phase Transition and Critical Thickness Study. *Phys. Rev. B - Condens. Matter Mater. Phys.* **2008**, *78* (10), 104112. https://doi.org/10.1103/PhysRevB.78.104112.

(4) Hu, S.; Alsubaie, A.; Wang, Y.; Lee, J. H.; Kang, K.-R.; Yang, C.-H.; Seidel, J. Poisson's Ratio of $BiFeO_3$ Thin Films: X-Ray Reciprocal Space Mapping under Variable Uniaxial Strain. *Phys. status solidi* **2017**, *214* (1), 1600356. https://doi.org/10.1002/pssa.201600356.

(5) Catalan, G.; Noheda, B.; McAneney, J.; Sinnamon, L. J.; Gregg, J. M. Strain Gradients in Epitaxial Ferroelectrics. *Phys. Rev. B - Condens. Matter Mater. Phys.* **2005**, *72* (2), 020102. https://doi.org/10.1103/PhysRevB.72.020102.

(6) Xu, G.; Hiraka, H.; Shirane, G.; Li, J.; Wang, J.; Viehland, D. Low Symmetry Phase in (001) $BiFeO_3$ Epitaxial Constrained Thin Films. *Appl. Phys. Lett.* **2005**, *86* (18), 1–3. https://doi.org/10.1063/1.1924891.

(7) Wu, X.; Kan, Y.; Lu, X.; Zhu, J.; Zhai, Y. Annealing Temperature Effect on Internal Strain and Ferroelectric Properties of $Bi_{3.25}La_{0.75}Ti_3O_{12}$ Thin Films. *Ferroelectrics* **2010**, *400* (1), 263–268. https://doi.org/10.1080/00150193.2010.505786.

(8) Johann, F.; Morelli, A.; Biggemann, D.; Arredondo, M.; Vrejoiu, I. Epitaxial Strain and Electric Boundary Condition Effects on the Structural and Ferroelectric Properties of $BiFeO_3$ Films. *Phys. Rev. B - Condens. Matter Mater. Phys.* **2011**, *84* (9), 094105. https://doi.org/10.1103/PhysRevB.84.094105.

(9) Liang, J.; Zhu, G.; Liu, P.; Luo, X.; Tan, C.; Jin, L.; Zhou, J. Synthesis and Characterization of Fe-

Doped β-Bi_2O_3 Porous Microspheres with Enhanced Visible Light Photocatalytic Activity. *Superlattices Microstruct.* **2014**, *72*, 272–282. https://doi.org/10.1016/j.spmi.2014.05.005.

(10) Nechache, R.; Harnagea, C.; Carignan, L.-P.; Gautreau, O.; Pintilie, L.; Singh, M. P.; Ménard, D.; Fournier, P.; Alexe, M.; Pignolet, A. Epitaxial Thin Films of the Multiferroic Double Perovskite Bi_2FeCrO_6 Grown on (100)-Oriented $SrTiO_3$ Substrates: Growth, Characterization, and Optimization. *J. Appl. Phys.* **2009**, *105* (6), 061621. https://doi.org/10.1063/1.3073826.

(11) Marchand, B.; Jalkanen, P.; Tuboltsev, V.; Vehkamäki, M.; Puttaswamy, M.; Kemell, M.; Mizohata, K.; Hatanpää, T.; Savin, A.; Räisänen, J.; et al. Electric and Magnetic Properties of ALD-Grown $BiFeO_3$ Films. *J. Phys. Chem. C* **2016**, *120* (13), 7313–7322. https://doi.org/10.1021/acs.jpcc.5b11583.

(12) Biesinger, M. C.; Brown, C.; Mycroft, J. R.; Davidson, R. D.; McIntyre, N. S. X-Ray Photoelectron Spectroscopy Studies of Chromium Compounds. *Surf. Interface Anal.* **2004**, *36* (12), 1550–1563. https://doi.org/10.1002/sia.1983.

(13) Biesinger, M. C.; Payne, B. P.; Grosvenor, A. P.; Lau, L. W. M.; Gerson, A. R.; Smart, R. S. C. Resolving Surface Chemical States in XPS Analysis of First Row Transition Metals, Oxides and Hydroxides: Cr, Mn, Fe, Co and Ni. *Appl. Surf. Sci.* **2011**, *257* (7), 2717–2730. https://doi.org/10.1016/j.apsusc.2010.10.051.

(14) Moulder, J. F.; Stickle, W. F.; Sobol, P. E.; Bomben, K. D. *Handbook of X-Ray Photoelectron Spectroscopy*; Chastain, J., Ed.; Perkin-Elmer Corporation: Eden Prairie, 1992.

(15) Sando, D.; Carrétéro, C.; Grisolia, M. N.; Barthélémy, A.; Nagarajan, V.; Bibes, M. Revisiting the Optical Band Gap in Epitaxial $BiFeO_3$ Thin Films. *Adv. Opt. Mater.* **2018**, *6* (2), 1700836. https://doi.org/10.1002/adom.201700836.